Slip tendency analysis, fault reactivation potential and induced seismicity in the Val d'Agri oilfield (Italy)

L. Vadacca[1], D. Rossi[1], A. Scotti[1], and M. Buttinelli[2].

[1]MOX, Department of Mathematics, Politecnico di Milano, Milan, Italy.
[2]Istituto Nazionale di Geofisica e Vulcanologia, Rome, Italy.

Key Points:

- Tectonic extension and wastewater injection in the Val d'Agri oilfield is simulated by numerical modeling.
- Fluid diffusion is strongly dependent on the active stress field and the geological structure in which fluids are injected.
- Different types of fault deformation act in the Val d'Agri oilfield as a response to fluid injection (mixed-mode fault slip behavior).

Corresponding author: Luigi Vadacca, `luigi.vadacca@polimi.it`

Abstract

The Val d'Agri basin hosts an oil-field, the largest in onshore Europe, and it is one of the areas of highest seismic hazard in Italy. In an unproductive marginal portion of the reservoir, wastewater is re-injected by a high-rate well. Since the beginning of re-injection in June 2006, a spatio-temporal correlation between microseismicity ($M_L \leq 2.2$) and wastewater injection has been observed (suggesting induced seismicity). In this paper we perform a slip-tendency analysis on the fault system involved in the induced seismicity through a coupled fluid-flow and geomechanical numerical model simulating the stress partitioning due to the tectonic forces and to the fluid injection. The model results show that the fluid diffusion is strongly dependent on the active stress field and the geological structure in which fluids are injected, which conditioned the occurrence of seismicity that aligned on a small portion of a NE-dipping fault. However, another fault located closer to the injection well and where no seismicity were detected, is the better well-oriented fault with the active stress field and, also, the one more susceptible to the pore pressure increase. These results suggest different types of fault deformation acting in the Val d'Agri oilfield as response to the fluid injection (i.e., a mixed-mode fault slip behavior). Understanding the stress partitioning in tectonically active regions where underground activities such as fluid injection are ongoing is fundamental to give strong constraints for the discrimination between natural and induced seismicity, and finally for a more reliable and robust definition of seismic hazard.

1 Introduction

Natural and anthropogenic alterations of the underground equilibrium can reactivate faults and cause earthquakes ((Grigoli et al., 2018; Keranen & Weingarten, 2018; Keranen et al., 2014; Ellsworth, 2013; Carder, 1945; Amos et al., 2014; Council, 2013) among others). Natural factors are related to the stress changes due to plate tectonics, while among the anthropogenic factors the most common are the stress changes induced by water table fluctuations and by the removal and the injection of fluids in the deep subsurface caused by hydrocarbons wastewater disposal, hydraulic fracturing, reservoir impoundment, extraction-injection of fluids associated to geothermal exploitation, and mining. Nuclear tests are reported to be able to induce from moderate to even large magnitude events as well (e.g.(Grigoli et al., 2017)). The seismicity associated with anthropogenic activities often raised concern not only within the scientific community but also within the society in general (Suckale, 2009; Grigoli et al., 2017). Since the astonishing evolution and dramatic increase of the underground activities in the last decades, especially with the increase of shale-gas-related activities, several cases of induced and triggered seismicity related to injection of wastewater from hydrocarbon exploitation into deep wells have been reported (e.g. the M_w5.7 Prague, Oklahoma and M_w5.3 Raton basin, Colorado sequences, (Keranen et al., 2013; Rubinstein et al., 2014)). The long-term water disposal by high-rate injection wells can in fact induce small-to-moderate earthquakes, remobilizing pre-existing faults as a consequence of pore pressure increase (Ellsworth, 2013; Evans, 1970; Healy et al., 1968; Raleigh et al., 1976). In such scenarios, the modeling of the interaction between fluid diffusion into the injection reservoirs and the existing discontinuities plays a fundamental role into the understanding of the mechanism of the induced seismicity, as well as a more reliable evaluation of the associated hazard (Juanes et al., 2016; J. B. Altmann et al., 2010; J. Altmann et al., 2014; Rutqvist et al., 2016; Rinaldi et al., 2015; Cappa & Rutqvist, 2011b, 2011a; Vilarrasa et al., 2016; Rinaldi et al., 2014).

In this contribution we explore such relationship integrating more than five years of data available from induced seismicity studies in the Val d'Agri oilfield, in Italy, (Improta et al., 2017; Diehl et al., 2017; Buttinelli et al., 2016; Clarke et al., 2014) to constrain a 3-D coupled fluid flow and geomechanical numerical model able to simulate the stress perturbations caused by wastewater injection. The model is built using a real topographic

surface, stratigraphic horizons and fault geometries deduced by local cross sections published by Buttinelli et al. (2016). In addition, the fault zones are modeled taking into account the differences between the hydro-mechanical properties of the damage zone and the fault core. An analysis of slip tendency is performed on the numerical results, with the objective of understanding which faults are more susceptible to the stress changes induced by the fluid injection and the possible physical mechanisms that induced the seismicity.

The paper is structured as follows: Sect. 2 describes the geological and seismological background of the region where the Val d'Agri oilfield is located; Sect. 3 lists the governing equations the numerical method and the data used to perform the coupled fluid flow and geomechanical simulations; Sect. 4 describes the results, including a sensitivity analysis of some uncertain variables (initial stress field, material properties), and also an analysis on the discrimination between the contribution of the tectonic forces and fluid-injection on the total slip tendency of the fault system; Sect. 5 contains the discussion of the numerical results, suggesting a fault deformation model acting in the Val d'Agri oilfield as response to the fluid injection; Sect. 6 draws the conclusions.

2 Geological and Seismological Background

The Val d'Agri (VDA) is a Quaternary basin developed within the southern Apennines thrust-and-fold belt (Figure 1), when an extensional phase followed a Mio-Pliocene compression (Brozzetti (2011); Patacca and Scandone (1989) among others). The general architecture of the area consists of a pile of thrust sheets mainly constituted by the calcareous sedimentary units of internal Apennine Platforms, the Lagonegro Basin and foredeep flysch deposits all together stacked over the Inner Apulian Platform limestones units (API , Figure 1B). The Late Pliocene-Early Pleistocene compressional phase is responsible for the development of N-to NW-trending thrusts (with antithetic back thrusts) mainly within the Apulian platforms (Noguera & Rea, 2000; Mazzoli et al., 2001; Shiner et al., 2004). The buried API is separated from the upper units by a mélange clayey layer that locally reaches a thickness of ∼1500 m. The recent VDA extensional basin is shaped by two active and opposite dipping, high-angle range-bounding fault systems: the Eastern Agri (EAFS) and the Monti della Maddalena (MMFS, Figure 1) (Cello et al., 2003; Maschio et al., 2005). Large normal-faulting earthquakes occurred along the axial sector of the southern Apennines and struck the VDA area, the last of which is the 1857 M_w7 event (Improta et al., 2014). Instrumental seismicity catalogues report only rare and sparse low-magnitude earthquakes ($M_L < 3$, Figure 1A; (Improta et al., 2015)). High-resolution studies of background seismicity evidenced that the shallow seismicity is spatially correlated with the southernmost fault segments of the MMFS (Figure 1B). Additional low-magnitude seismicity was related to the seasonal variations of the Pertusillo water impoundment located a few kilometers to the South of the oilfield (Valoroso et al., 2009, 2011) (Figure 1A). Moreover, since June 2006 a spatio-temporal relation between microseismicity ($M_L \leq 2.2$) and the wastewater re-injection by a high-rate well (60 k to 80 k m^3/month; Costa Molina 2, CM2; Figure 2) into an unproductive marginal portion of the reservoir has been observed (Stabile et al., 2014; Improta et al., 2015, 2017; Buttinelli et al., 2016). Here, hypocenters align on a NE-dipping back-thrust (fault F1; Figure 2b) located few kilometers from the well (Buttinelli et al., 2016). The induced events are mainly located on the NW side of a NE-SW transfer zone that, hence, could act as a structural barrier (Caine et al., 1996) for fluid diffusion into the reservoir. However, a controversial aspect is that no significant events are recorded along the principal thrust fault (fault F2, Figure 2b) located very close (100 m) to injection well and with similar dip to the back-thrust ($50°-60°$). Fault orientation, pore pressure, stress field and sliding friction coefficient are the parameters that affect the frictional reactivation of brittle faults (Anderson, 1905; Sibson, 1985). In the last years a large amount of geological, geophysical and seismological data have been produced by induced seismicity

studies (Johann et al., 2018; Goebel et al., 2017; Barbour et al., 2017; Buttinelli et al., 2016; Norbeck & Horne, 2016; Improta et al., 2015; Guglielmi et al., 2015; Ellsworth, 2013; Majer et al., 2007). These studies have given a great contribution to the understanding of the physical processes triggered by fluid-structure interaction in active fault zones. Frictional laboratory experiments on fault rock samples have shown that the style of deformation (e.g. stick-slip or creeping) can change in presence of fluids (Scuderi & Collettini, 2016). In addition, high-precision seismicity locations coupled with the interpretation of high-resolution seismic profiles have allowed to understand the spatial-temporal evolution of the permeability inside complex fault systems (Buttinelli et al., 2016; Improta et al., 2015).

3 Model Description

The geometry consists of a block of $9 \times 12 \times 9$ km with the surface topography on the top and different layers representing the main hydrological units: the permeable storage aquifer (L3), the low-permeable cap rocks (L2) and the upper and basal aquifers (L1 and L4 respectively; Figure 3a). The storage aquifer is cut by a fault system that is characterized by four $40-60°$ dipping faults and a subvertical transfer zone (Figure 3b). The computational domain is characterized entirely by a frictional-porous-elastic rheology (Vadacca et al., 2018; ABAQUS, 2013).

The model domain (Ω) contains the fault cores as embedded surfaces (Γ). On the two sides of the Γ surfaces, quantities like pore pressure (p_f) and displacement ($\mathbf{u}$) can take different (and thus discontinuous) values. On the fault, when referring to values of a variable on the hanging wall side, the superscript '$^+$' will be used. Similarly, '$^-$' will denote the foot wall. At each time, we can identify two different portions of Γ, depending on the status of each point on Γ with respect to the stress. The part of the surface that is sliding is indicated by Γ_S, the part that remains locked is indicated by Γ_L. The system of equation that is solved numerically is:

$$
\begin{cases}
\nabla \cdot (\boldsymbol{\sigma}'(\boldsymbol{u}) + p_f \boldsymbol{\delta}) + \rho_b \boldsymbol{g} = \mathbf{0} & \text{in } \Omega \quad (1a) \\
\dfrac{1}{M}\dfrac{\partial p_f}{\partial t} + \dfrac{\partial \epsilon_v(\boldsymbol{u})}{\partial t} - \rho_f \cdot \left(\dfrac{\boldsymbol{k}}{\mu_f} \nabla p_f - \rho_f \boldsymbol{g} \right) = \rho_f f & \text{in } \Omega \quad (1b) \\
\mathbf{u}^+ - \mathbf{u}^- = \overline{\mathbf{d}} & \text{on } \Gamma_L \quad (1c) \\
\boldsymbol{\tau} = -\mu_\Gamma \sigma_n' \dfrac{\dot{\mathbf{d}}}{\|\dot{\mathbf{d}}\|} & \text{on } \Gamma_S \quad (1d) \\
-\dfrac{\boldsymbol{k}}{\mu_f} \nabla p_f^{\pm} \cdot \mathbf{n}_\Gamma = \dfrac{\kappa_c}{\mu_f}(p_f^+ - p_f^-) & \text{on } \Gamma \quad (1e)
\end{cases}
$$

Eq.(1a) is the momentum conservation equation, and contains the effective stress tensor $\boldsymbol{\sigma}'(\boldsymbol{u})$ ($\boldsymbol{\sigma}' = \boldsymbol{\sigma} - p_f \boldsymbol{\delta}$, where $\boldsymbol{\sigma}$ is the total stress), the gravitational acceleration $\boldsymbol{g}$ and the density of the bulk ρ_b. Here, $\boldsymbol{\delta}$ is the unit tensor. The dependence of $\boldsymbol{\sigma}'$ on $\boldsymbol{u}$ is expressed, for the poro-elastic medium, as the double inner product of the fourth order modulus tensor $\boldsymbol{\mathcal{C}}^{dr}$ and the strain $\boldsymbol{\epsilon}$:

$$
\boldsymbol{\sigma}' = \boldsymbol{\mathcal{C}}^{dr} : \boldsymbol{\epsilon}(\mathbf{u}), \quad (2)
$$

where the ij-th element of $\boldsymbol{\epsilon}$ is defined as:

$$
\epsilon_{ij} = \frac{1}{2}\left(\frac{\partial u_i}{\partial x_j} + \frac{\partial u_j}{\partial x_i} \right), \quad (3)
$$

while $\boldsymbol{\mathcal{C}}^{dr}$, for an isotropic and elastic response can be written as a function of the Young modulus E and Poisson ratio ν:

Table 1: Hydro-mechanical properties of the layers. Rock density ρ_s, Young modulus E, Poisson ratio ν, Bulk modulus K_f, porosity ϕ and permeability k.

Layer	ρ_s[kg/m^3]	E[GPa]	ν	K_f[GPa]	ϕ	k[m^2]
L1	2520	32.16	0.30	2.2	0.1	10^{-15}
L2	2610	49.16	0.28	2.2	0.08	10^{-19}
L3	2830	84.35	0.26	2.2	0.05	10^{-14}
L4	2830	84.35	0.26	2.2	0.049	10^{-16}

Table 2: Hydro-mechanical properties of the fault zones. Rock density ρ_s, Young modulus E, Poisson ratio ν, Bulk modulus K_f, porosity ϕ, damage zone k_d and fault core permeabilities k_c.

Layer	ρ_s[kg/m^3]	E[GPa]	ν	K_f[GPa]	ϕ	k_d[m^2]	k_c[m^2]
Fault zone	2550	41.39	0.30	2.2	0.052	10^{-13}	10^{-19}

$$\mathcal{C}^{dr}_{ijkl} = \frac{E}{2(1+\nu)}(\delta_{ik}\delta_{jl} + \delta_{il}\delta_{jk}) + \frac{E}{3}\left(\frac{1}{(1-2\nu)} - \frac{1}{(1+\nu)}\right)\delta_{ij}\delta_{kl}. \tag{4}$$

Eq.(1b) comes from the conservation of the fluid mass, where the fluid flow velocity is expressed by the Darcy equation. The first and second left hand side terms are accounting for the variation in the rock porosity: M takes into account the bulk compressibility of the medium, and the time derivative of the volumetric strain ($\epsilon_v = \nabla \cdot \boldsymbol{u}$) takes into account the deformation of the skeleton. On the right hand side, $\rho_f f$ is the injection rate of the fluid. Eq.(1c) and Eq.(1d) describe the two possible conditions for the fault displacement.

The two equations are derived from Amonton's law, which states that the ratio of the shear stress over the normal stress of a sliding fault cannot exceed the friction coefficient,

$$\frac{\tau}{\sigma'_n} \leq \mu_s \tag{5}$$

where $\sigma'_n = (\boldsymbol{\sigma}\boldsymbol{n}) \cdot \boldsymbol{n}$ is the effective normal stress ($\boldsymbol{n}$ is the normal vector to the fault surface; σ_n is positive in compression), $\tau = \boldsymbol{\sigma}\boldsymbol{n} - \sigma_n \boldsymbol{n}$ is the shear stress, and μ_s is the sliding friction coefficient. The fault thus is locked for $\tau/\sigma'_n < \mu_s$ while it slides when the condition (5) is verified as an equality. This translates in the constitutive equations (1c) and (1d): a fixed value $\overline{\mathbf{d}}$ for the displacement jump is imposed in the case of locked fault (Eq. 1c), while on the sliding portion of the fault the stress is kept as the limit tangential traction prescribed by Amonton's law (Eq 1d) along the direction of the displacement time derivative $\dot{\mathbf{d}}$, i.e. the slip velocity. Given the dramatic change in the stress tensor that a fault that starts sliding can generate, and the discontinuous behavior caused by the threshold μ_s, the numerical solution of the system must be carried out iteratively in order to reach a consistent result that accounts for the coupled effects. The last equation, Eq.(1e), comes from the requirement of a continuous fluid velocity through the fault surface. The flow tangential to the surface Γ, considered its negligible width and low permeability, is neglected. The hydro-mechanical properties of the different lithological layers and fault zones are shown in table 1 and 2 respectively. Based on inequality (5) we

define the slip tendency (ST), as the ratio of shear stress to normal stress acting on the plane of weakness:

$$ST = \tau/\sigma'_n. \tag{6}$$

The slip tendency indicates if a fault is in a stable or unstable state of stress: if $ST < \mu_s$ the state of stress is stable and no slip occurs along the fault plane. Otherwise, if $ST \geq \mu_s$ the strength of the fault is overcome and slip starts to propagate along the fault plane (Vadacca et al., 2018; Moeck et al., 2009; Collettini & Trippetta, 2007; Lisle & Srivastava, 2004; Morris et al., 1996). We use a static friction constitutive model where μ_s is constant and equal to 0.6, which is a typical value for faults within carbonate rocks (Scuderi & Collettini, 2016). The static friction model is strongly simplified if compared to the more realistic constitutive models as the rate- and state-dependent friction law (Dieterich, 1979; Ruina, 1983; Marone, 1998) that allow to describe the fault behavior along the entire seismic cycle. However, in this work we are more interested in understanding the stress field evolution along the faults before slip occurs. The finite element software ABAQUS (ABAQUS, 2013) is used to carry out the numerical simulations. The volume is meshed by 3.3 million of tetrahedral elements with characteristic length varying from 100 meter in the storage aquifer to 500 meter away from it. The nodes along the fault surfaces are split in two following the split-node technique as described in Vadacca et al. (2018). This condition is necessary in order to model the deformation along the faults via frictional contacts. While fault cores are represented by frictional contacts with zero thickness, the damage zones are instead represented by a 100 meter thick layer parallel to the fault surfaces. A crucial point for study cases located in active tectonic regions is the description of the stress partitioning operated by tectonic forces on the fault system. The simulation takes care of this aspect by including an additional step to initialize the stress field. Indeed, the simulation is performed in three subsequent steps. In the first one, we apply a gravitational loading on the entire domain (geostatic step) considering a hydrostatic initial pore pressure. The stress field resulting from this stage is defined as uniaxial strain reference frame (Engelder, 1993) and characterized by the following effective principal vertical stress:

$$S'_v = \rho_s g z - \rho_w g z, \tag{7}$$

where ρ_s is the density of the rocks, ρ_w is the density of water, g is the gravity acceleration and z is the depth. The principal horizontal stresses can be calculated as follows:

$$S'_H = S'_h = \left(\frac{\nu}{1-\nu}\right) S'_v, \tag{8}$$

where ν is Poisson's ratio. In this first step, the boundary conditions applied to the model are the following: the upper boundary (topographic surface) is free to move in all the directions, while the lateral boundaries of the mesh and the bottom are kept fixed in the perpendicular direction. After this first step, the system is at equilibrium and the solution is used as the initial condition for the second step. In the second step we stretch the model (crustal extension is simulated) for 600 years, applying a constant horizontal velocity of 3 $mm\,yr^{-1}$ on the NE lateral boundary (Figure 3), according to the present-day strain rate and kinematics of the region (Hunstad et al., 2003; Ferranti et al., 2008). At the end of the second step we obtain a normal faulting stress regime where $S'_v > S'_H > S'_h$ (Anderson, 1905) with the minimum principal horizontal stress axis S'_h oriented NE-SW (Mariucci & Montone, 2016) (Figure 4a-b). The orientation and magnitude of the principal stress axis is crucial in the slip tendency analysis. For this reason this step is fundamental to obtain a realistic present-day stress field. Indeed, without the extension step, the stress field resulting by the geostatic step would be of normal faulting type but with a strong rotation of horizontal principal stress axis due to boundary effects of the model. After the second step, the system is at equilibrium and the solution is used as

the initial condition for the third step (injection step). Fluid injection is simulated by a source term applied at one node at a depth of almost 3100 m into the storage aquifer, close to the F2 fault zone (3b). The volume rates of injected water follow the average trend reported in Stabile et al. (2014) and Improta et al. (2015): linear increase of 500 m^3/day to 1800 m^3/day from June 2006 to April 2008; 1800 m^3/day from April 2008 to June 2010; linear increase of 1800 m^3/day to 2400 m^3/day from June 2010 to December 2013 (Figure 6A).

Different model configurations are considered. In the Model-1 (M1) the initial stress field and the hydro-mechanical properties have the reference values as stated above in this section. In addition, in the third step (injection step) the tectonic loading is turned off in order to only evaluate the fluid-injection contribution on the stress perturbations in the storage aquifer. In the Model-2 (M2) and Model-3 (M3) we consider two different initial stress fields by changing the duration of the tectonic extension in the second step (200 and 400 years respectively). In this way, it is possible to investigate the effects of the initial stress field on the slip tendency values computed on the faults. In the Model-4 (M4), the storage aquifer and fault damage zones permeability values are one order of magnitude smaller than the reference model, in accordance to the range of permeability values for fractured limestones ((Improta et al., 2015) and references therein). Finally, we run two additional models. In Model-5 (M5) we turned on the tectonic loading in the third step but considered null fluid injection rates. In Model-6 (M6), tectonics and fluid-injection contributions are considered together. In this way, we can discriminate between the tectonic and the fluid-injection contributions to the variation of the total slip-tendency.

4 Model Results

4.1 Reference model

Figure 5a-b shows the spatial distribution of the pore pressure change on the fault system for two time snapshots of the M1 (reference model). Pore pressure change for a given time is computed as the difference between the pore pressure at that time and the pore pressure at the time $t = 0$ before the first injection step. At time $t = 3.8$ years (half the simulation), the effects of fluid diffusion are located mainly on the faults F1, F2 and F5. The maximum pore pressure increase of 0.8 MPa is located at the top of the fault F2, in proximity to the injection point. On F1, a maximum pore pressure increase of 0.55 MPa occurs on the bottom of the fault in proximity of the conjunction with fault F2. The fault F5 reaches the maximum values of pore pressure increase close to the top tip line like F1, but with smaller values (0.5 MPa). At end of the simulation ($t = 7.6$ years) the pore pressure increase reaches a peak value of 1.3 MPa on the fault F2. On the fault F1, the pore pressure front propagates from the bottom to the top, reaching a maximum pore pressure increase of 0.89 MPa. It is observable that the fluids cannot diffuse in the normal direction to the fault F5 due to the low permeability of the fault core, but they propagate in the direction tangential to the fault F5 through the more permeable damage zone. With this mechanism, the F3 and F4 faults are also reached by the fluids and their pore pressure gradient is perturbed. Figure 5c-d shows the spatial distribution of the slip tendency change for the same time frames described above. The slip tendency change for a given time is computed, similarly to pore pressure, as the difference between the slip tendency at that time and the slip tendency at the time $t = 0$. The obtained value is then divided for the fault friction coefficient ($\mu = 0.6$). In this way, the value of slip tendency change gives information about the fluid injection contribution to the fault stability. The distribution of the slip tendency change reflects closely the pore pressure one. The larger values are located mainly along the F2 with maximum values of 0.011 close to the injection point at t=3.8 year and 0.02 at the end of the simulation. F1 present larger values in the central and lower part of the fault with values of ~ 0.005 at $t = 3.8$ year and values of ~ 0.01 at the end of the simulation ($t = 7.6$ year). In general, our model gives low values of slip tendency change, even on the faults

F1 and F2 that are well-oriented with the active stress field and are the closest to the injection point. F5 presents very low values of slip tendency change due to the fact that it is poorly oriented with respect to the stress field.

Figures 6a-d show the time evolution of the changes in pore pressure, effective normal stress, shear stress and slip tendency for a set of 9 points. The points are divided in 3 groups of 3, and each group is located on a different fault: F1, F2 and F5. The points on same fault are chosen at three different depths: 3000 m, 3400 m and 3800 m (see Figure 3b for the locations). Figure 6a shows the pore pressure change compared with the fluid injection rates (black line). The pore pressure increase follows the injection rates for all points, with a more direct effect for points closer to the injection point (id F2b-M1, green square in the graph). It is important to observe that even if the points F1a-M1 and F1b-M1 are located closer to the injection point, the largest increase of pore pressure on the F1 fault is observed at the deepest point (F1c-M1, blue triangles). This is due to the larger permeability of the F2-fault damage zone with respect to the storage aquifer, so that the damage zone acts as a preferential pathway for the fluid migration: the injected fluids leak into the F2 damage zone, but due to the low permeability of the fault core they cannot migrate across the fault plane and thus propagate in the tangential direction reaching the F1-fault in depth. From that the fluids move into F1 damage zone and propagate upward. For the F5 fault zone, the fluid diffusion process is similar to the F2-fault one, but with a larger pore pressure increase in the shallower part of the fault. Figure 6b shows the time evolution of the effective normal stress change. Depending on the pore pressure front, the effective normal stress decreases everywhere with a maximum drop of 0.92 MPa at the end of the simulation, close to the injection point (on the F2-fault). The shear stress is also affected (Figure 6c) by the fluid injection, although that variation is small compared to the effective normal stress one. The change $\Delta\tau$ assumes positive values (shear stress increase) on the F5 transfer zone and negative values (Shear stress decrease) on the F1 and F2 dipping faults.

4.2 Initial stress field effects

In this section we compare the results of the model M1, whose results are shown in the previous section, with those of the models M2 and M3 (Figure 7) that differ by the initial stress fields as they have been subjected to a different duration of the tectonic extension phase during the second step of the simulation (200 and 400 years respectively). By doing this comparison, we expect to assess the influence of the initial stress field on the stability of the fault once the injection starts. We remark that in the M1 we consider a duration of the tectonic extension of 600 years which is consistent with the occurrence time of moderate earthquakes for the main seismogenetic faults in the Val D'Agri region (DISS-Working-Group, 2018). This amount of extension also resulted in the alignment of the minimum principal stress axis in the NE-SW direction (similarly to what is evinceable from the borehole breakouts data; 2,4). In order to make the comparison in Figure 7 we show the data for the middle sample point (point b located at a depth of 3400 m, see Figure 3) for each of the previously analyzed faults (F1, F2 and F5).

We observe that the variations of pore pressure, effective normal and shear stress are similar for all the models considered. Larger differences between the models can be observed in the slip tendency change, in particular on the F1 and F2 faults (Figure 7d). In fact, in M1 these faults present larger values of slip tendency change than in M2 and M3. In particular we observe that the larger is the duration of the tectonic extension the larger is the value of slip tendency. This shows that not only the absolute value of slip tendency is larger in the case of larger initial extension, as it can be easily expected, but that also the relative change of slip tendency due to the injection is increased as well. This is due to the fact that, when extension is applied on the faults F1 and F2, it increases slightly the shear stress and reduces the normal stress, and the relative importance that

the perturbation in the pore pressure has on the effective normal stress increases, and in turn this influences the slip tendency because of Equation (6).

4.3 Effects of the storage aquifer and fault damage zone permeability changes

The values of permeability play a major role in the fluid diffusion process. For this reason, in Figure 8 we compare the results of the model M1 (reference model) with those of M4, where the storage aquifer and fault damage zones permeability values are decreased of one order of magnitude (10^{-15} and 10^{-14} respectively), consistently with the range of permeability values for fractured limestones ((Improta et al., 2015) and references therein). All the other parameters, including the initial stress field are the same of M1.

In Figure 8a we observe that the pore pressure increases in the M4, in particular for the point located on the F2 fault (F2b-M4), which is closer to the injection point and encased between surfaces of low permeability. Here, the pore pressure changes reaches values of 7.8 MPa at the end of the simulation versus a maximum of 1.3 MPa in the M1. The effective normal stress decreases accordingly to the increase of pore pressure, reaching the value of -4.5 MPa for the point on F2 (F2b-M4; Figure 8b). Note that also the values of shear stress change significantly (Figure 8c) as a consequence of the decrease in permeability in the material around the faults (Zoback, 2007). In M4, the slip tendency increases of one order of magnitude with respect to M1, with maximum values close to 0.1 (Figure 8d).

4.4 Discriminating between fluid-induced, tectonic and total slip tendency

In all the numerical models previously described, the tectonic forces were switched off during the third step (injection phase), in order to isolate the contribution of fluid injection on fault stability. Geomechanical modeling gives us the possibility to discriminate and quantify the tectonic contribution from the fluid-injection one on the slip tendency changes. For this reason, in Figure 9 we compare the results of M1 with those of the models M5 and M6. In M5, the tectonic loading is active in the third step but no fluid injection is simulated. Whereas, in M6, we simulate both the tectonic loading and fluid injection. Figures 9a-b-c-d show the time evolution of the changes of pore pressure, effective normal stress, shear stress, and slip tendency for the mid sample point of each fault. In Figure 9a it is possible to see that the pore pressure change reaches the same values for the M1 and M6, whereas M5 present null variations as no fluid is injected from the well. In Figure 9b and Figure 9c the effects of the tectonic loading on the variation of the normal and shear stress along the faults are well visible. These variations reach maximum values in the range of 0.05-0-08 MPa. As shown in Figure 9d, the values of slip tendency change in M6 is approximately the sum of the values in M1 and M5. The combined contributions of the tectonic loading and fluid injection bring the F1 fault to reach a maximum slip tendency change of 0.024. A deviation of about one order of magnitude between the maximum slip tendency change of M1 (0.019) and M5 (0.005) shows that fluid injection can be an important factor in the seismicity generation (induced seismicity; Improta et al. (2015)).

5 Discussion

5.1 Fault zone architecture and fluid diffusion process

The results of the numerical simulation give important information on the possible induced seismicity mechanisms active during fluid injection in the Val d'Agri oilfield and on the seismic potential of the fault system affected by the fluid diffusion process. Coupled fluid flow-geomechanical simulations represent a key instrument to understand

the hydro-mechanical interaction between geological structure and fluid diffusion in the subsurface (Juanes et al., 2016; Rutqvist et al., 2016; Rinaldi et al., 2015; J. Altmann et al., 2014; Cappa & Rutqvist, 2011b, 2011a). In this work, we underline the importance of modeling the fault zone as a multilayer (damage zone-fault core) characterized by different hydro-mechanical properties. This approach has been also adopted successfully by Vilarrasa et al. (2016) and Rinaldi et al. (2014) to define the best location where to inject CO_2 in relation to the fault stability. In the Val d'Agri oilfield, the injection of wastewater close to the F2 fault affects the diffusion of fluids into the F1 fault zone, triggering possible earthquakes. Indeed, the fault core, characterized by low permeability, acts like a geological barrier (Caine et al., 1996) for fluid migration in the NE direction (normal to the fault plane). On the contrary, the damage zone allows the migration of fluids in the direction tangential to the fault plane. Given the structural setting of the fault system, the F1 and F2 damage zones intersect at almost 4 km of depth representing a unique conduit for the fluid circulation. This aspect is well evident in Figure 5 where the pore pressure increase occurs from the bottom to the top of the F1 fault plane as consequence of the continuous inflow of fluid from the F2 damage zone. As a consequence, the slip tendency also increases (Figure 5d). The fluid diffusion process modeled in this work is in a good agreement with the correlation detected between fluid injection rates and microseismicity (Improta et al., 2015) and the observed migration of seismicity from the deeper to the shallower part of the F1 fault zone (Buttinelli et al., 2016). Another important result concerns the role of the F5 transfer zone (Figure 3b) in the compartmentalization of the fluids in the storage aquifer. This fault is misoriented (Anderson, 1905; Sibson, 1985) with the active stress field in the region (Figure 4b) and this means that it is less likely to reactivate than the other dipping faults. This is shown in Figure 6d where the maximum values of slip tendency change obtained on the F5 fault are of 0.002. However, even if the F5 fault is far from the reactivation, its role as hydrological barrier is fundamental in the redistribution of the stress in the storage aquifer due to fluid injection. Indeed, the transfer zone prevents the migration of fluids toward S in the direction normal to the fault plane. In this way, pore pressure increases mainly on the N-side of the fault as shown in Figure 5 and this can explain why the large amount of microseismicity is concentrated on that side of the fault (Figure 2a).

5.2 Hypothesis of mixed-mode fault slip behavior

There are some discrepancies between observation and the presented numerical results. Figure 10 shows that the maximum values of slip tendency change ($ST_{max} = 0.025$) are located on the top of F2 fault where no induced seismicity is observed (Figure 10). Indeed the larger amount of microseismicity is well aligned on the F1 fault back-thrust where the maximum values of ST ($ST_{max} = 0.012$) are smaller compared to the F2 fault. The lack of seismicity on the shallower part of the F2 fault can be justified by a mechanical model (Figure 10) where the F2 fault is supposed to react with an aseismic creeping deformation, while the F1 fault reacts with a seismic creeping deformation. If we hypothesize that the F2 fault is characterized by velocity strengthening behavior (Dieterich, 1979; Ruina, 1983), an increase in fluid pressure would promote fault creep. Then, the stress transfer generated by the aseismic slip along the F2 fault, together with fluid diffusion into the damage zone, would reactivate the F1 fault in depth with a mixed-mode slip behavior: fault creep and microseismicity on fault patches that could be more prone to develop frictional instabilities. Finally, earthquakes would propagate upward into the F1 fault zone with the same combined effect of stress transfer and fluid diffusion described for the F2 fault. As described by Scuderi and Collettini (2016), for carbonate-bearing faults unstable fault slip might result from velocity weakening gouge at higher temperature (Verberne et al., 2015), sharp and localized slipping zones (Tesei et al., 2014) or strongly cemented fault portions (Carpenter et al., 2014). There is at least one case where this behavior has been observed: Guglielmi et al. (2015) describe an experiment along a well instrumented natural carbonate-bearing fault, where the increase of fluid pressure,

induced by fluid injection, promoted aseismic slip along the fault, inducing microseismicity on adjacent regions as a secondary effect. In addition, recent studies based on rock deformation experiments have shown that the slip mode can change depending on the fluid pressure into the fault zone (Scuderi & Collettini, 2016). In particular, with the increase of pore pressure, the friction rate parameter (a-b) evolves from velocity strengthening to velocity neutral behavior and the critical slip distance (D_c) decreases contributing to a transition from stable sliding to frictional instability (Scuderi & Collettini, 2016). The proposed mechanical model can be also used to justify some intriguing features that characterize the first days of the fluid injection. In fact, Buttinelli et al. (2016) and Improta et al. (2015, 2017) have shown that the Costa Molina 2 injection well case study is characterized by a quasi-instantaneous onset of induced seismicity (i.e., hours from initiation of injection). In addition, the swarms recorded during the initial, daily injection tests (initial 10 days of injection) that cluster on the basal portion of fault F2, have a rate that correlates strictly to hourly injection data (pressure and rate) with a time delay of a few hours. In Figure 11 we compare the slip tendency change with the microseismicity in the first four weeks of the fluid injection. In the first week, we observe that the seismic swarm is located in the deepest part of the F2 fault where the values of slip tendency change are initially lower (11a). The swarm in the depth can be due to dynamic effects that start acting as soon as the injection begins, due to an increase of local permeability parallel to the F2 fault plane as the fault itself moves because of aseismic creep. Successively (11b-c), the microseismicity migrates in the shallower layers along the F1 fault where a slip tendency increase is observed (11d). Even if the initial dynamic effects are not included, our model results show a strict correlation between the amount of seismic events and the simulated slip tendency changes (Figure 12). In fact, we observe that the slope of the slip tendency change curves are more steeps in the first week (Figure 12a) where the larger amount of seismicity is detected (Figure 12d).

5.3 Seismic potential induced by fluid injection in active tectonic regions

The numerical results show that the fluid injection (with or without the contribute of the tectonic loading) induces small variations in the values of slip tendency during the 7.6 years of the simulation (Figure 5, 10). Specifically, the contribution of fluid injection alone amounts to a maximum slip tendency increase of 0.019 on the F2 fault. Considering also the tectonic loading, the maximum slip tendency reaches values of 0.024, again on the F2 fault. These values are far from the condition of fault reactivation ($ST/\mu = 1.0$), considering a sliding friction coefficient of $\mu = 0.6$ (that is typical for carbonate-bearing faults (Scuderi & Collettini, 2016)). In this work, we analyze the slip tendency only in terms of variation due to the uncertainty of some variables as the sliding friction coefficient and initial stress field. For this reason, the seismic potential induced by fluid injection should be discussed with caution. In fact, sliding friction can change depending on the rate and state parameters (Dieterich, 1979; Ruina, 1983; Scholz, 1989; Marone, 1998), which in turn change depend on the pore pressure conditions (Scuderi & Collettini, 2016). In addition, the real stress field is unknown, and even if it has been simulated in agreement with spatial data on large regional scale (Mariucci & Montone, 2016), detailed analysis including local borehole breakouts and other well data could better constrain it. Notwithstanding the limits of the tectonic extension simulation in the model, it still gives information that are useful in the understanding of the stress partitioning within the fault system. This aspect is very important because, as shown in Figure 7, the maximum slip tendency increment due to fluid injection occurs in the area with the largest values of slip tendency due to the extension, suggesting a strict correlation between fluid propagation and the inherited tectonic stress field.

In addition to the aspects described above, there is another process than can affect the stress field and hence the slip tendency on the faults and that must be considered. The injection zone is located at the southern margin of the oilfield. Following Improta et al. (2017), a very large amount of oil and brine has been removed since the late '90s

from the southern part of the hydrocarbon reservoir, specifically from high production wells located to the W of the injection well and a few kilometers apart from the induced seismicity cluster. Several modelling studies have shown the importance of considering the combined effect of fluid production and injection in reproducing properly the pore pressure (e.g the Cavone oilfield case study investigated by Juanes et al. (2016)). The effects of fluid production on the fault stability are an actual and intriguing problem still under discussion by the scientific community. In fact, if on one hand fluid production can stabilize the faults as a direct effect of the effective normal stress increase (see equation 6), on the other hand that can generate a local shear stress increase as an indirect effect of the poroelastic response of the material (J. Altmann et al., 2014, 2014). This complex effect is strictly dependent on the distance of the fluid source and on the architecture of the fault system. For this reason the application of geomechanical models to realistic cases is going to become essential. At the present time, fluid production data in Val d'Agri oilfield are not published and availables. These data if available could improve the representativity of our simulations of a sensible amount.

6 Conclusions

The Val d'Agri oil field is located in an area with high seismic risk. From 2006 the area has been interested by induced seismicity due to fluid injection in an unproductive well. This makes this area a great opportunity to shed new lights on the discrimination between natural and induced seismicity, as well as to study of the interaction between injected fluids and geological structures. The numerical model results show that fluid diffusion is strongly dependent on the active stress field and the geological structure in which fluids are injected, which conditioned the occurrence of seismicity that aligned on a strict portion of a back-thrust. Slip tendency analysis shows that the thrust fault (F2 fault) located below the back-thrust and closer to the injection point with respect to the back-thrust is the one more susceptible to the pore pressure increase. The mismatch with the fluid injection-induced microseismicity could suggest a prevalent aseismic slip behavior associated to this fault and a mixed-mode slip behavior along the backthrust. We also modeled an important role played by other vertical structures present into the injection reservoir, which enhanced the compartmentalization favoring the overpressuring of the system and leading the directivity of the pore pressure diffusion into the the reservoir volumes. Such analysis is of high importance since it might give strong constraints for the discrimination between natural and induced seismicity. This is much more necessary in active tectonic areas as the Southern Apennines where underground human activities are ongoing, also for a more reliable and robust definition of seismic hazard considering human induced seismicity.

Acknowledgments

The authors thank Luca Formaggia for the fruitful discussions about the fault reactivation modeling, and Luca Paglieri for the maintenance of the MOX-HPC facilities. The authors have no real or perceived conflicts of interest related to this research. All numerical simulation data used in this work are stored in the Politecnico di Milano repository, located at https://re.public.polimi.it/handle/11311/1121540 website.

References

ABAQUS. (2013). Theory manual, version 6.13 [Computer software manual]. Providence, Rhode Island.

Altmann, J., Müller, B., Müller, T., Heidbach, O., Tingay, M., & Weißhardt, A. (2014). Pore pressure stress coupling in 3d and consequences for reservoir stress states and fault reactivation. *Geothermics*, *52*, 195 - 205. doi: https://doi.org/10.1016/j.geothermics.2014.01.004

Altmann, J. B., Müller, T. M., Müller, B. I., Tingay, M. R., & Heidbach, O. (2010). Poroelastic contribution to the reservoir stress path. *International Journal of Rock Mechanics and Mining Sciences*, *47*(7), 1104 - 1113. doi: https://doi.org/10.1016/j.ijrmms.2010.08.001

Amos, C. B., Audet, P., Hammond, W. C., Burgmann, R., Johanson, I. A., & Blewitt, G. (2014). Uplift and seismicity driven by groundwater depletion in central california. *Nature*, *509*, 483-486. doi: 10.1038/nature13275

Anderson, E. (1905). The dynamics of faulting. *Transactions of the Edinburgh Geological Society*, *8*(3), 387–402. doi: 10.1144/transed.8.3.387

Barbour, A. J., Norbeck, J. H., & Rubinstein, J. L. (2017, 05). The Effects of Varying Injection Rates in Osage County, Oklahoma, on the 2016 Mw 5.8 Pawnee Earthquake. *Seismological Research Letters*, *88*(4), 1040-1053. doi: 10.1785/0220170003

Brozzetti, F. (2011). The campania-lucania extensional fault system, southern italy: A suggestion for a uniform model of active extension in the italian apennines. *Tectonics*, *30*(5). doi: 10.1029/2010TC002794

Buttinelli, M., Improta, L., Bagh, S., & Chiarabba, C. (2016). Inversion of inherited thrusts by wastewater injection induced seismicity at the val d'agri oilfield (italy). *Scientific Reports*, *6*. doi: https://doi.org/10.1038/srep37165

Caine, J. S., Evans, J. P., & Forster, C. B. (1996, 11). Fault zone architecture and permeability structure. *Geology*, *24*(11), 1025-1028. doi: 10.1130/0091-7613(1996)024⟨1025:FZAAPS⟩2.3.CO;2

Cappa, F., & Rutqvist, J. (2011a). Impact of co2 geological sequestration on the nucleation of earthquakes. *Geophysical Research Letters*, *38*(17). doi: 10.1029/2011GL048487

Cappa, F., & Rutqvist, J. (2011b). Modeling of coupled deformation and permeability evolution during fault reactivation induced by deep underground injection of co2. *International Journal of Greenhouse Gas Control*, *5*(2), 336 - 346. doi: https://doi.org/10.1016/j.ijggc.2010.08.005

Carder, D. S. (1945, 10). Seismic investigations in the Boulder Dam area, 1940-1944, and the influence of reservoir loading on local earthquake activity*. *Bulletin of the Seismological Society of America*, *35*(4), 175-192.

Carpenter, B. M., Scuderi, M. M., Collettini, C., & Marone, C. (2014). Frictional heterogeneities on carbonate-bearing normal faults: Insights from the monte maggio fault, italy. *Journal of Geophysical Research: Solid Earth*, *119*(12), 9062-9076. doi: 10.1002/2014JB011337

Cello, G., Tondi, E., Micarelli, L., & Mattioni, L. (2003). Active tectonics and earthquake sources in the epicentral area of the 1857 basilicata earthquake (southern italy). *Journal of Geodynamics*, *36*(1), 37 - 50. (Active Faults: Analysis, Processes and Monitoring) doi: https://doi.org/10.1016/S0264-3707(03)00037-1

Clarke, H., Eisner, L., Styles, P., & Turner, P. (2014). Felt seismicity associated with shale gas hydraulic fracturing: The first documented example in europe. *Geophysical Research Letters*, *41*(23), 8308-8314. doi: 10.1002/2014GL062047

Collettini, C., & Trippetta, F. (2007). A slip tendency analysis to test mechanical and structural control on aftershock rupture planes. *Earth and Planetary Science Letters*, *255*(3), 402 - 413. doi: https://doi.org/10.1016/j.epsl.2007.01.001

Council, N. R. (2013). *Induced seismicity potential in energy technologies*. Washington, DC: The National Academies Press. doi: 10.17226/13355

Diehl, T., Kraft, T., Kissling, E., & Wiemer, S. (2017). The induced earthquake sequence related to the st. gallen deep geothermal project (switzerland): Fault reactivation and fluid interactions imaged by microseismicity. *Journal of Geophysical Research: Solid Earth*, *122*(9), 7272-7290. doi: 10.1002/2017JB014473

Dieterich, J. H. (1979). Modeling of rock friction: 1. experimental results and constitutive equations. *Journal of Geophysical Research: Solid Earth*, *84*(B5), 2161-2168. doi: 10.1029/JB084iB05p02161

DISS-Working-Group. (2018). Database of individual seismogenic sources (diss), version 3.2.1: A compilation of potential sources for earthquakes larger than m 5.5 in italy and surrounding areas. *Istituto Nazionale di Geofisica e Vulcanologia*. doi: 10.6092/INGV.IT-DISS3.2.1

Ellsworth, W. L. (2013). Injection-induced earthquakes. *Science*, *341*(6142). doi: 10.1126/science.1225942

Engelder, T. (1993). *Stress regimes in the lithosphere*. Princeton University Press.

Evans, D. M. (1970, 01). The Denver Area Earthquakes and the Rocky Mountain Arsenal Disposal Well*. In *Engineering Seismology*. Geological Society of America. doi: 10.1130/Eng-Case-8.25

Ferranti, L., Oldow, J. S., D'Argenio, B., Catalano, R., Lewis, D., Marsella, E., ... Sulli, A. (2008). Active deformation in Southern Italy, Sicily and southern Sardinia from GPS velocities of the Peri-Tyrrhenian Geodetic Array (PTGA). *Bollettino Della Società Geologica Italiana*, *127*(2), 299-316.

Goebel, T., Weingarten, M., Chen, X., Haffener, J., & Brodsky, E. (2017). The 2016 mw5.1 fairview, oklahoma earthquakes: Evidence for long-range poroelastic triggering at ¿40 km from fluid disposal wells. *Earth and Planetary Science Letters*, *472*, 50 - 61. doi: https://doi.org/10.1016/j.epsl.2017.05.011

Grigoli, F., Cesca, S., Priolo, E., Rinaldi, A. P., Clinton, J. F., Stabile, T. A., ... Dahm, T. (2017). Current challenges in monitoring, discrimination, and management of induced seismicity related to underground industrial activities: A european perspective. *Reviews of Geophysics*, *55*(2), 310-340. doi: 10.1002/2016RG000542

Grigoli, F., Cesca, S., Rinaldi, A. P., Manconi, A., López-Comino, J. A., Clinton, J. F., ... Wiemer, S. (2018). The november 2017 mw 5.5 pohang earthquake: A possible case of induced seismicity in south korea. *Science*, *360*(6392), 1003–1006. doi: 10.1126/science.aat2010

Guglielmi, Y., Cappa, F., Avouac, J.-P., Henry, P., & Elsworth, D. (2015). Seismicity triggered by fluid injection–induced aseismic slip. *Science*, *348*(6240), 1224–1226. doi: 10.1126/science.aab0476

Healy, J. H., Rubey, W. W., Griggs, D. T., & Raleigh, C. B. (1968). The denver earthquakes. *Science*, *161*(3848), 1301–1310. doi: 10.1126/science.161.3848.1301

Hunstad, I., Selvaggi, G., D'Agostino, N., England, P., Clarke, P., & Pierozzi, M. (2003). Geodetic strain in peninsular italy between 1875 and 2001. *Geophysical Research Letters*, *30*(4). doi: 10.1029/2002GL016447

Improta, L., Bagh, S., De Gori, P., Valoroso, L., Pastori, M., Piccinini, D., ... Buttinelli, M. (2017). Reservoir structure and wastewater-induced seismicity at the val d'agri oilfield (italy) shown by three-dimensional vp and vp/vs local earthquake tomography. *Journal of Geophysical Research: Solid Earth*, *122*(11), 9050-9082. doi: 10.1002/2017JB014725

Improta, L., De Gori, P., & Chiarabba, C. (2014). New insights into crustal structure, cenozoic magmatism, co2 degassing, and seismogenesis in the southern apennines and irpinia region from local earthquake tomography. *Journal of Geophysical Research: Solid Earth*, *119*(11), 8283-8311. doi: 10.1002/2013JB010890

Improta, L., Valoroso, L., Piccinini, D., & Chiarabba, C. (2015). A detailed analysis of wastewater-induced seismicity in the val d'agri oil field (italy). *Geophysical Research Letters*, *42*(8), 2682-2690. doi: 10.1002/2015GL063369

Johann, L., Shapiro, S. A., & Dinske, C. (2018). The surge of earthquakes in central oklahoma has features of reservoir-induced seismicity. *Scientific Reports*, *8*(1), 11505. doi: 10.1038/s41598-018-29883-9

Juanes, R., Jha, B., Hager, B. H., Shaw, J. H., Plesch, A., Astiz, L., ... Frohlich, C. (2016). Were the may 2012 emilia-romagna earthquakes induced? a coupled flow-geomechanics modeling assessment. *Geophysical Research Letters*, *43*(13), 6891-6897. doi: 10.1002/2016GL069284

Keranen, K. M., Savage, H. M., Abers, G. A., & Cochran, E. S. (2013, 06). Potentially induced earthquakes in Oklahoma, USA: Links between wastewater injection and the 2011 Mw 5.7 earthquake sequence. *Geology*, *41*(6), 699-702. doi: 10.1130/G34045.1

Keranen, K. M., & Weingarten, M. (2018). Induced seismicity. *Annual Review of Earth and Planetary Sciences*, *46*(1), 149-174. doi: 10.1146/annurev-earth-082517-010054

Keranen, K. M., Weingarten, M., Abers, G. A., Bekins, B. A., & Ge, S. (2014). Sharp increase in central oklahoma seismicity since 2008 induced by massive wastewater injection. *Science*, *345*(6195), 448–451. doi: 10.1126/science.1255802

Lisle, R. J., & Srivastava, D. C. (2004, 07). Test of the frictional reactivation theory for faults and validity of fault-slip analysis. *Geology*, *32*(7), 569-572. doi: 10.1130/G20408.1

Majer, E. L., Baria, R., Stark, M., Oates, S., Bommer, J., Smith, B., & Asanuma, H. (2007). Induced seismicity associated with enhanced geothermal systems. *Geothermics*, *36*(3), 185 - 222. doi: https://doi.org/10.1016/j.geothermics.2007.03.003

Mariucci, M. T., & Montone, P. (2016). The new release of the Italian contemporary stress map. *Geophysical Journal International*, *205*(3), 1525-1531. doi: 10.1093/gji/ggw100

Marone, C. (1998). Laboratory-derived friction laws and their application to seismic faulting. *Annual Review of Earth and Planetary Sciences*, *26*(1), 643-696. doi: 10.1146/annurev.earth.26.1.643

Maschio, L., Ferranti, L., & Burrato, P. (2005). Active extension in val d'agri area, southern apennines, italy: implications for the geometry of the seismogenic belt. *Geophysical Journal International*, *162*(2), 591-609. doi: 10.1111/j.1365-246X.2005.02597.x

Mazzoli, S., BARKHAM, S., CELLO, G., GAMBINI, R., MATTIONI, L., SHINER, P., & TONDI, E. (2001). Reconstruction of continental margin architecture deformed by the contraction of the lagonegro basin, southern apennines, italy. *Journal of the Geological Society*, *158*(2), 309–319. doi: 10.1144/jgs.158.2.309

Moeck, I., Kwiatek, G., & Zimmermann, G. (2009). Slip tendency analysis, fault reactivation potential and induced seismicity in a deep geothermal reservoir. *Journal of Structural Geology*, *31*(10), 1174 - 1182. doi: https://doi.org/10.1016/j.jsg.2009.06.012

Morris, A., Ferrill, D. A., & Henderson, D. (1996, 03). Slip-tendency analysis and fault reactivation. *Geology*, *24*(3), 275-278. doi: 10.1130/0091-7613(1996)024⟨0275:STAAFR⟩2.3.CO;2

Noguera, A., & Rea, G. (2000). Deep structure of the campanian–lucanian arc (southern apennine, italy). *Tectonophysics*, *324*(4), 239 - 265. Retrieved from `http://www.sciencedirect.com/science/article/pii/S0040195100001372` doi: https://doi.org/10.1016/S0040-1951(00)00137-2

Norbeck, J. H., & Horne, R. N. (2016). Evidence for a transient hydromechanical and frictional faulting response during the 2011 mw 5.6 prague, oklahoma earthquake sequence. *Journal of Geophysical Research: Solid Earth*, *121*(12), 8688-8705. doi: 10.1002/2016JB013148

Patacca, E., & Scandone, P. (1989). Post-tortonian mountain building in the apennines. the role of the passive sinking of a relic lithospheric slab. *In A. Boriani, M. Bonafede, G.B. Piccardo, and G.B. Vai, Eds., The Lithosphere in Italy, Atti dei Convegni dei Lincei*, *80*, 157-176.

Raleigh, C. B., Healy, J. H., & Bredehoeft, J. D. (1976). An experiment in earthquake control at rangely, colorado. *Science*, *191*(4233), 1230–1237. doi: 10.1126/science.191.4233.1230

Rinaldi, A. P., Jeanne, P., Rutqvist, J., Cappa, F., & Guglielmi, Y. (2014). Effects of fault-zone architecture on earthquake magnitude and gas leakage related to co2 injection in a multi-layered sedimentary system. *Greenhouse Gases: Science and Technology*, *4*(1), 99-120. doi: 10.1002/ghg.1403

Rinaldi, A. P., Vilarrasa, V., Rutqvist, J., & Cappa, F. (2015). Fault reactivation during co2 sequestration: Effects of well orientation on seismicity and leakage. *Greenhouse Gases: Science and Technology*, *5*(5), 645-656. doi: 10.1002/ghg.1511

Rubinstein, J. L., Ellsworth, W. L., McGarr, A., & Benz, H. M. (2014, 09). The 2001–Present Induced Earthquake Sequence in the Raton Basin of Northern New Mexico and Southern Colorado. *Bulletin of the Seismological Society of America*, *104*(5), 2162-2181. doi: 10.1785/0120140009

Ruina, A. (1983). Slip instability and state variable friction laws. *Journal of Geophysical Research: Solid Earth*, *88*(B12), 10359-10370. doi: 10.1029/JB088iB12p10359

Rutqvist, J., Rinaldi, A. P., Cappa, F., Jeanne, P., Mazzoldi, A., Urpi, L., ... Vilarrasa, V. (2016). Fault activation and induced seismicity in geological carbon storage – lessons learned from recent modeling studies. *Journal of Rock Mechanics and Geotechnical Engineering*, *8*(6), 789 - 804. doi: https://doi.org/10.1016/j.jrmge.2016.09.001

Scholz, C. H. (1989). Mechanics of faulting. *Annual Review of Earth and Planetary Sciences*, *17*(1), 309-334. doi: 10.1146/annurev.ea.17.050189.001521

Scuderi, M. M., & Collettini, C. (2016). The role of fluid pressure in induced vs. triggered seismicity: insights from rock deformation experiments on carbonates. *Scientific Reports*, *6*. doi: https://doi.org/10.1038/srep24852

Shiner, P., Beccacini, A., & Mazzoli, S. (2004). Thin-skinned versus thick-skinned structural models for apulian carbonate reservoirs: constraints from the val d'agri fields, s apennines, italy. *Marine and Petroleum Geology*, *21*(7), 805 - 827. (Oil and Gas in Compressional Belts) doi: https://doi.org/10.1016/j.marpetgeo.2003.11.020

Sibson, R. H. (1985). A note on fault reactivation. *Journal of Structural Geology*, *7*(6), 751 - 754. doi: https://doi.org/10.1016/0191-8141(85)90150-6

Stabile, T. A., Giocoli, A., Perrone, A., Piscitelli, S., & Lapenna, V. (2014). Fluid injection induced seismicity reveals a ne dipping fault in the southeastern sector of the high agri valley (southern italy). *Geophysical Research Letters*, *41*(16), 5847-5854. doi: 10.1002/2014GL060948

Suckale, J. (2009). Chapter 2 - induced seismicity in hydrocarbon fields. In *Advances in geophysics* (Vol. 51, p. 55 - 106). Elsevier. doi: https://doi.org/10.1016/S0065-2687(09)05107-3

Tesei, T., Collettini, C., Barchi, M. R., Carpenter, B. M., & Stefano, G. D. (2014). Heterogeneous strength and fault zone complexity of carbonate-bearing thrusts with possible implications for seismicity. *Earth and Planetary Science Letters*, *408*, 307 - 318. doi: https://doi.org/10.1016/j.epsl.2014.10.021

Vadacca, L., Colciago, C. M., Micheletti, S., & Scotti, A. (2018). Effects of the anisotropy of the fault zone permeability on the timing of triggered earthquakes: Insights from 3d-coupled fluid flow and geomechanical deformation modeling. *Pure and Applied Geophysics*, *175*(12), 4131–4144. doi: 10.1007/s00024-018-1936-4

Valoroso, L., Improta, L., Chiaraluce, L., Di Stefano, R., Ferranti, L., Govoni, A., & Chiarabba, C. (2009). Active faults and induced seismicity in the val d'agri area (southern apennines, italy). *Geophysical Journal International*, *178*(1), 488-502. doi: 10.1111/j.1365-246X.2009.04166.x

Valoroso, L., Improta, L., De Gori, P., & Chiarabba, C. (2011). Upper crustal structure, seismicity and pore pressure variations in an extensional seismic belt through 3-d and 4-d vp and vp/vs models: The example of the val d'agri area (southern italy). *Journal of Geophysical Research: Solid Earth*, *116*(B7). doi: 10.1029/2010JB007661

Verberne, B. A., Niemeijer, A. R., De Bresser, J. H. P., & Spiers, C. J. (2015). Mechanical behavior and microstructure of simulated calcite fault gouge sheared at 20–600 c: Implications for natural faults in limestones. *Journal of Geophysical Research: Solid Earth*, *120*(12), 8169-8196. doi: 10.1002/2015JB012292

Vilarrasa, V., Makhnenko, R., & Gheibi, S. (2016). Geomechanical analysis of the influence of co2 injection location on fault stability. *Journal of Rock Mechanics and Geotechnical Engineering*, *8*(6), 805 - 818. doi: https://doi.org/10.1016/j.jrmge.2016.06.006

Zoback, M. D. (2007). *Reservoir geomechanics*. Cambridge University Press. doi: 10.1017/CBO9780511586477

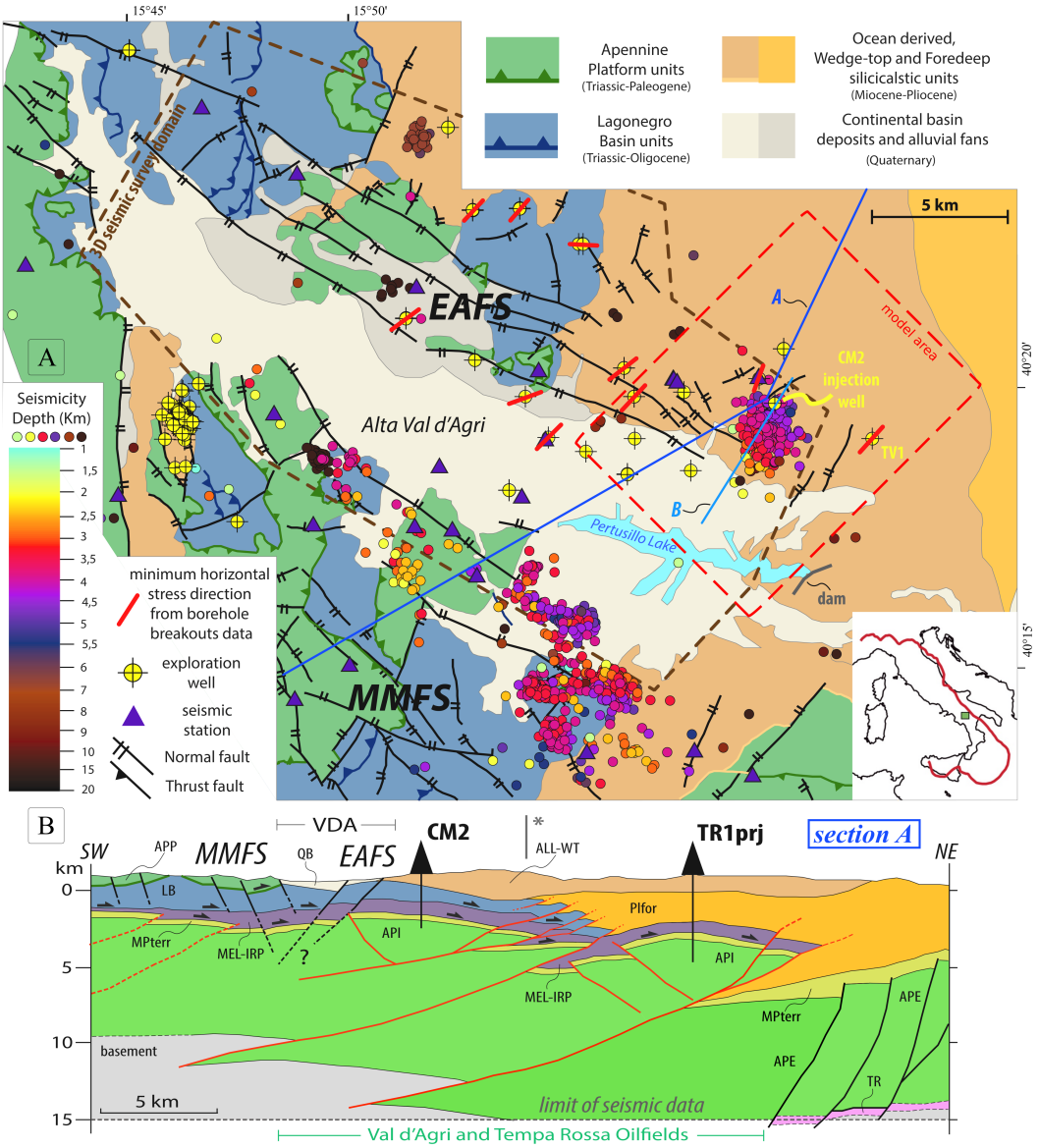

Figure 1: (A) Geological map of the Val d'Agri (VDA) region reporting: seismic stations (triangles), the 2001– 2014 seismicity as a function of hypocentral depth (coloured circles), exploration wells (yellow circles). The red lines on wells indicate minimum horizontal stress directions inferred from borehole breakouts. Blue lines report the traces of 2 sections shown in Figure 1B and 2B. The dashed square show the area of the numerical models. (B) Schematic geological section across the VDA illustrating the axial and external sectors of the southern Apennines. TR-Permo-Triassic clastic sequences. APE-External Apulia Platform (Mesozoic-Tertiary), API-Internal Apulia Platform (Mesozoic-Tertiary); MPterr- Late Miocene-Lower Pliocene terrigenous unconformable deposits covering the API; MEL-IRP: melange layer (Late Miocene-Lower Pliocene) and undifferentiated Miocene Flysch; LB-Lagonegro basin units (Mesozoic-Paleogene); APP-internal Apennine Platform (Mesozoic-Tertiary); EFC-marly-calcareous sequences and Miocene flysch deposits (External Flysch Complex); ALL-WT-allochthonous units of the Internal Apenninic Nappe (Albidona Formation, Eocene-Miocene) and related wedge-top deposits (Gorgoglione Formation, Middle-Upper Miocene); QB-VDA Quaternary basin; CM2-Costa Molina 2 well; TR1-Tempa Rossa 1 well; TV1-Tempa del Vento 1 well. The geometries of the faults with ids 1 to 5 are used in the numerical simulation (modified after Buttinelli et al., 2016).

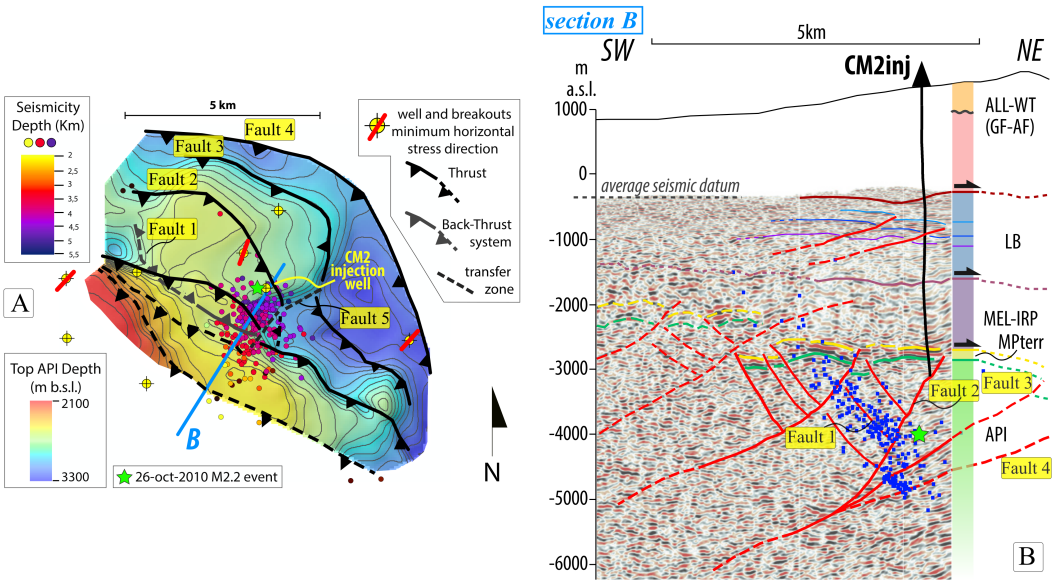

Figure 2: (A) Structural map of the top of API in the injection area and distribution of the 2006–2014 induced seismicity (In both panels the green star depicts the ML 2.0 event accompanied by the focal mechanism). The map shows the main SW-dipping reverse faults, the sub-vertical transverse fault (dashed line), the NE-dipping back-thrust related to the induced seismicity and deep wells with associated borehole breakouts. Section traces in blue color. (B) Interpretation of the depth converted vertical slice extracted from the 3D seismic volume tied to the CM2 well. The section trace is showed in Figure 1A (section B). The blue dots depict hypocenters of the 2006–2014 seismicity occurred close to the CM2 well. Main seismographic unit code references can be found in Figure 1 (modified after Buttinelli et al. (2016)).

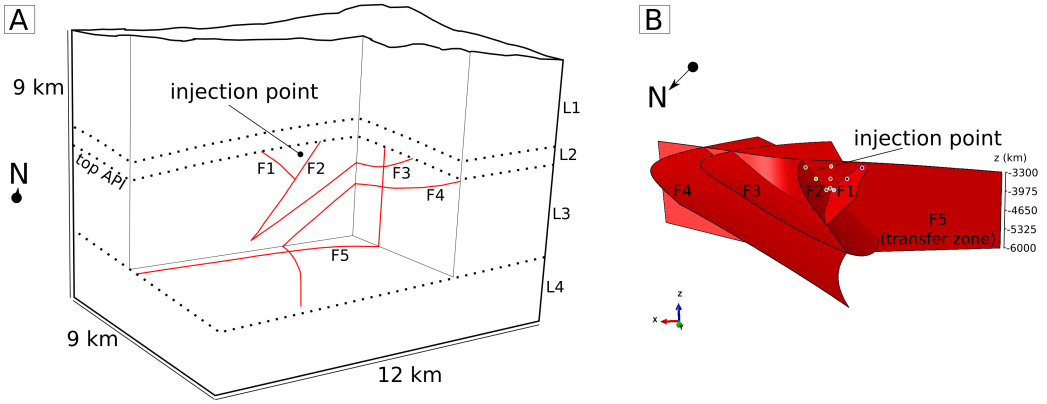

Figure 3: (A) Computational domain. L1, L2, L3 and L4 represent the main hydrological units: the permeable storage aquifer (L3), the low-permeable cap rocks (L2) and the upper and basal aquifers (L1 and L4 respectively). The black point located between the F1 and F2 fault represents the fluid injection point. Faults are shown in red. (B) Fault system geometry used in the numerical simulation. The colored dots on F1, F2 and F5 represent the location where different physical quantities are analyzed in the next sections.

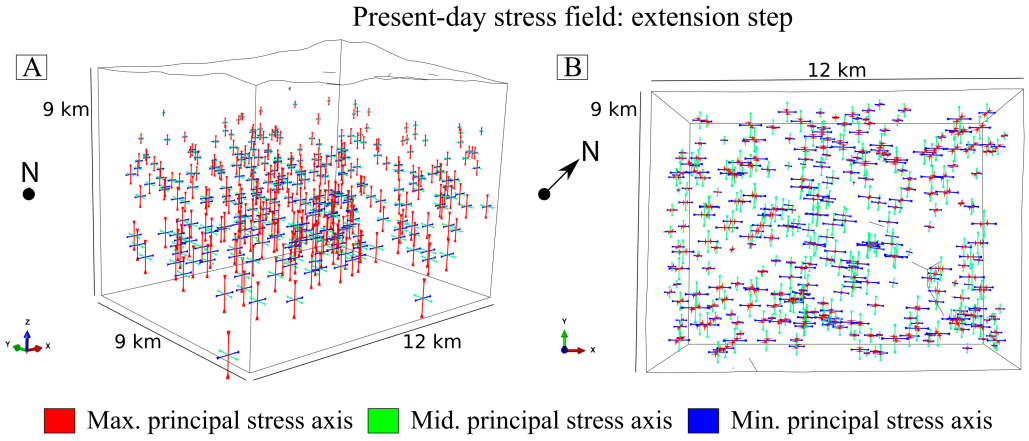

Figure 4: Stress field computed at the extension step (A-B). In red, green and blue are shown the maximum, middle and minimum principal stress axes respectively. The maximum principal stress axis is vertical consistently with the extensional stress regime in the Val d'Agri region. Also, the maximum principal stress increases with the depth in compliance with the lithostatic load. Note that, at the end of the extension step, the minimum horizontal stress axis is well oriented in the NE-direction, and this is consistent with the well breakouts directions shown in Figure 2A.

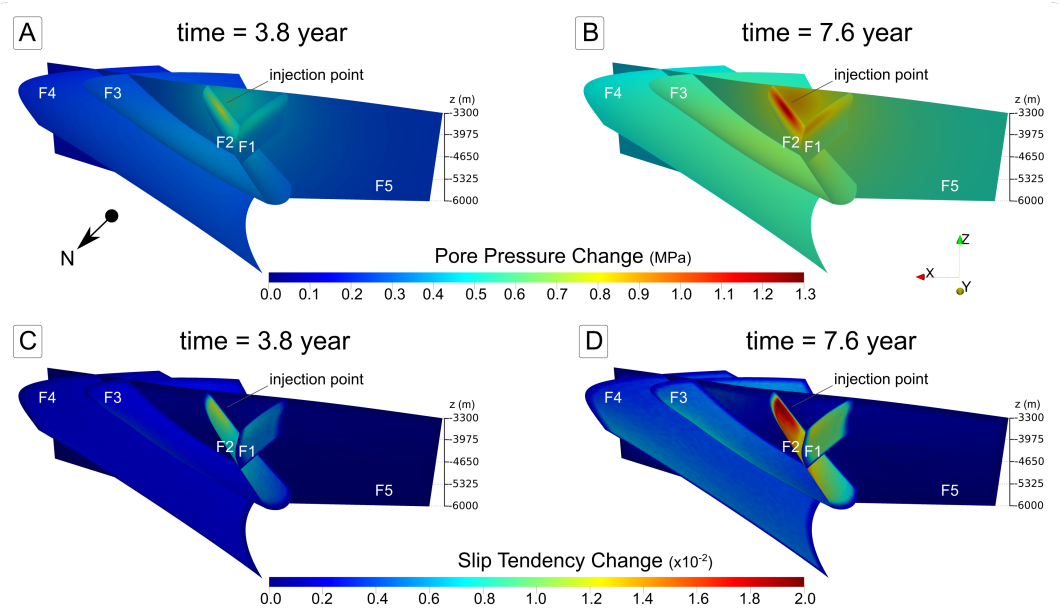

Figure 5: Spatial distribution of the pore pressure change on the fault system for two time snapshots: (A) 3.8 year; (B) 7.6 years (the end of the simulated injection phase). The pore pressure change for a given time is computed as the difference between the pore pressure at that time and the pore pressure at the time t=0 just preceding the first injection step. Spatial distribution of the slip tendency change on the fault system for two time snapshots: (A) 3.8 year; (B) 7.6 years (the end of the simulated injection phase). Similarly to the pore pressure change, the slip tendency change for a given time is computed as the difference between the slip tendency at that time and the slip tendency at the time t=0. The difference is then divided for the friction coefficient ($\mu = 0.6$).

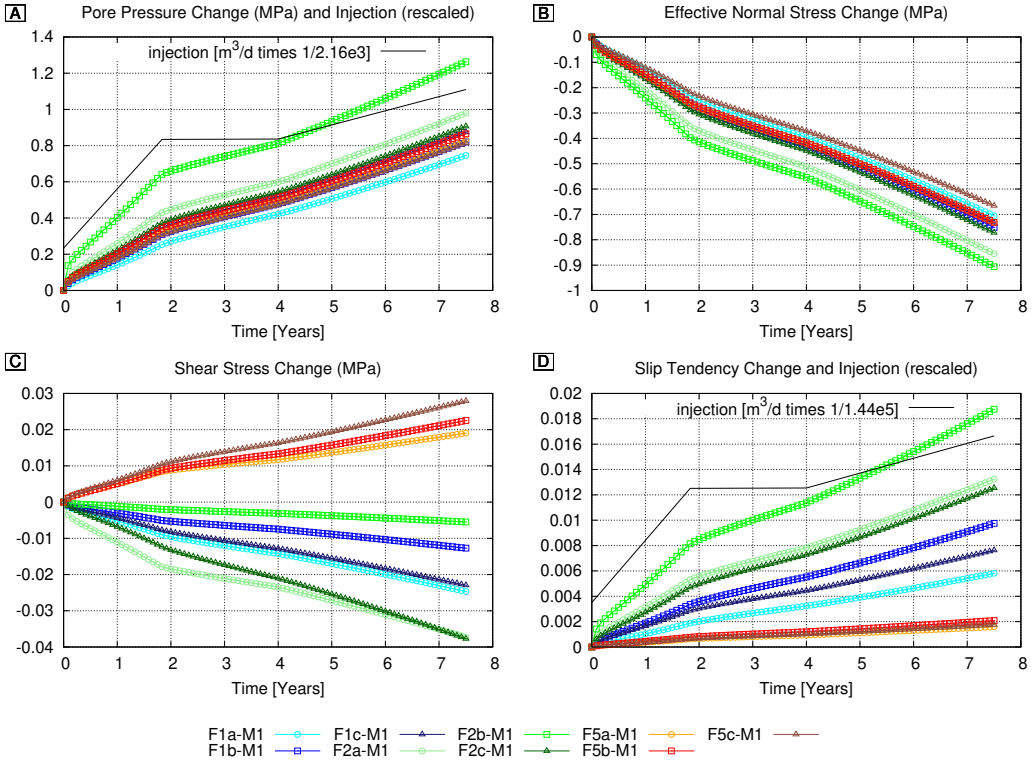

Figure 6: Time evolution of the changes in (A) pore pressure, (B) effective normal stress, (C) shear stress and (D) slip tendency for a set of 9 points. Of those, 3 points are located on the fault F1 (light-blue, blue and dark blue lines), 3 are on the fault F2 (light green, green ad dark green lines) and the last 3 are on the fault F5 (indicated by orange, red and plum lines). For each set of points on a fault, one is at about 3000m, another at ∼3400m and the last one at ∼3800m (see Figure 3b for the locations). The black line represents the fluid injection rates, rescaled in order to fit with the other quantities in the graph.

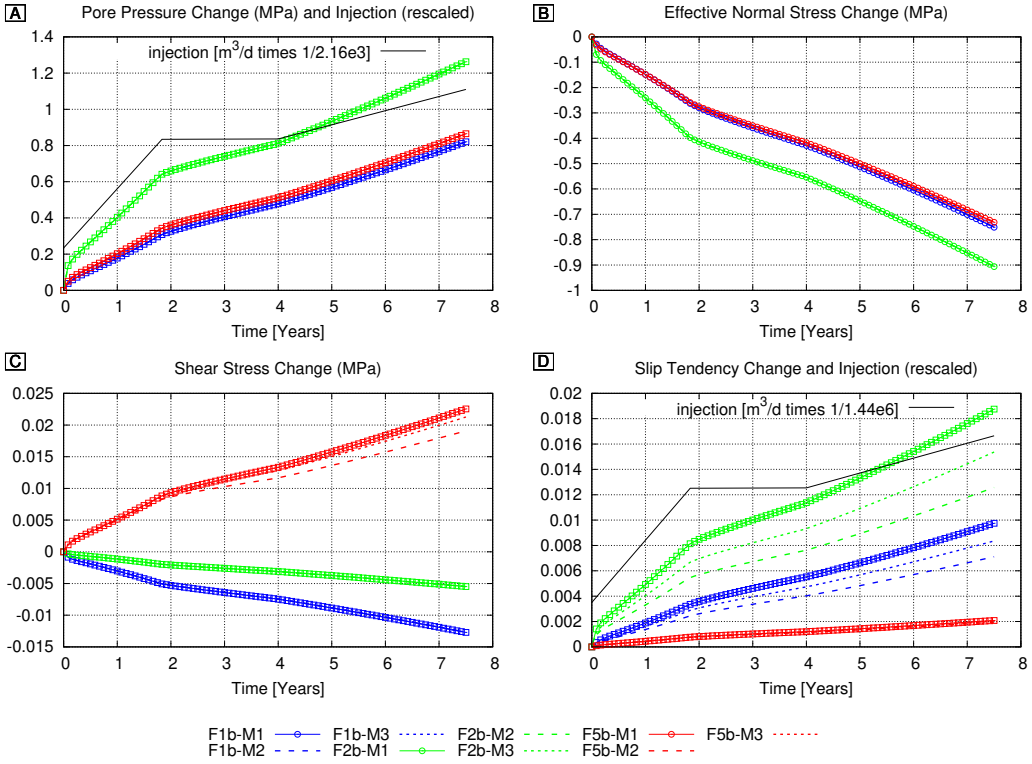

Figure 7: Comparison between the Model-1 (M1), Model-2 (M2) and Model-3 (M3) results. The time evolution of the changes in (A) pore pressure, (B) effective normal stress, (C) shear stress and (D) slip tendency is here shown only for the point b on the F1, F2 and F5 faults (see Figure 3b for the locations). The black line represents the fluid injection rates, rescaled in order to fit with the other quantities in the graph.

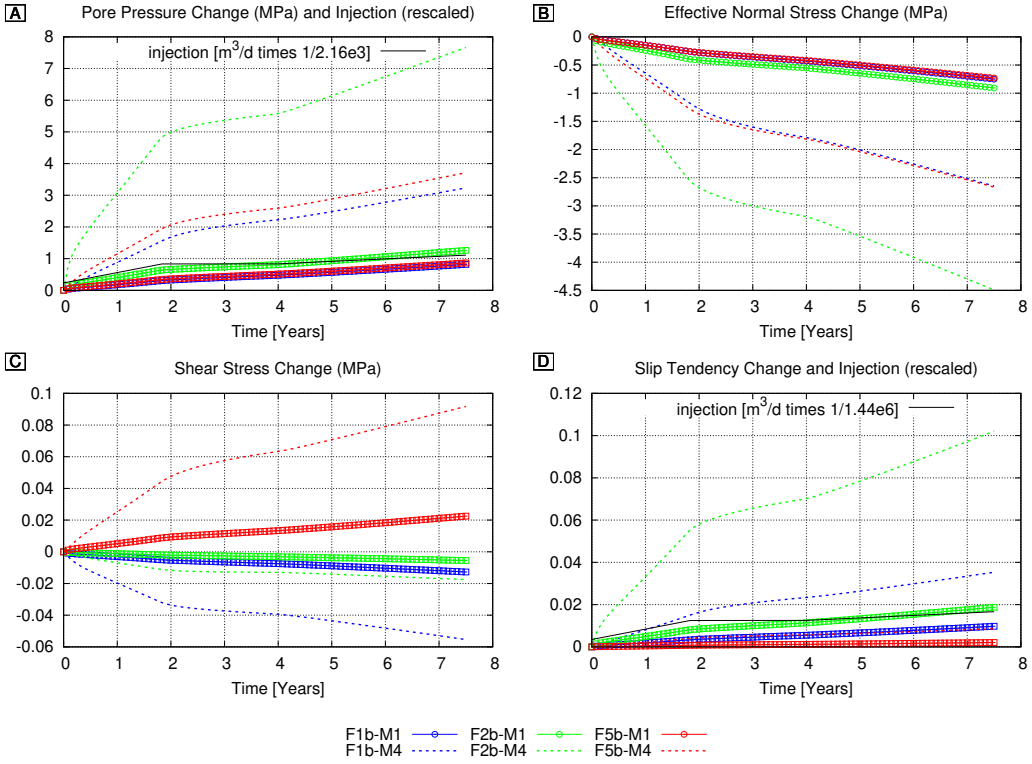

Figure 8: Comparison between the Model-1 (M1) and Model-4 (M4) results. The time evolution of the changes in (A) pore pressure, (B) effective normal stress, (C) shear stress and (D) slip tendency is here shown only for the point b on the F1, F2 and F5 faults (see Figure 3b for the locations). The black line represents the fluid injection rates, rescaled in order to fit with the other quantities in the graph.

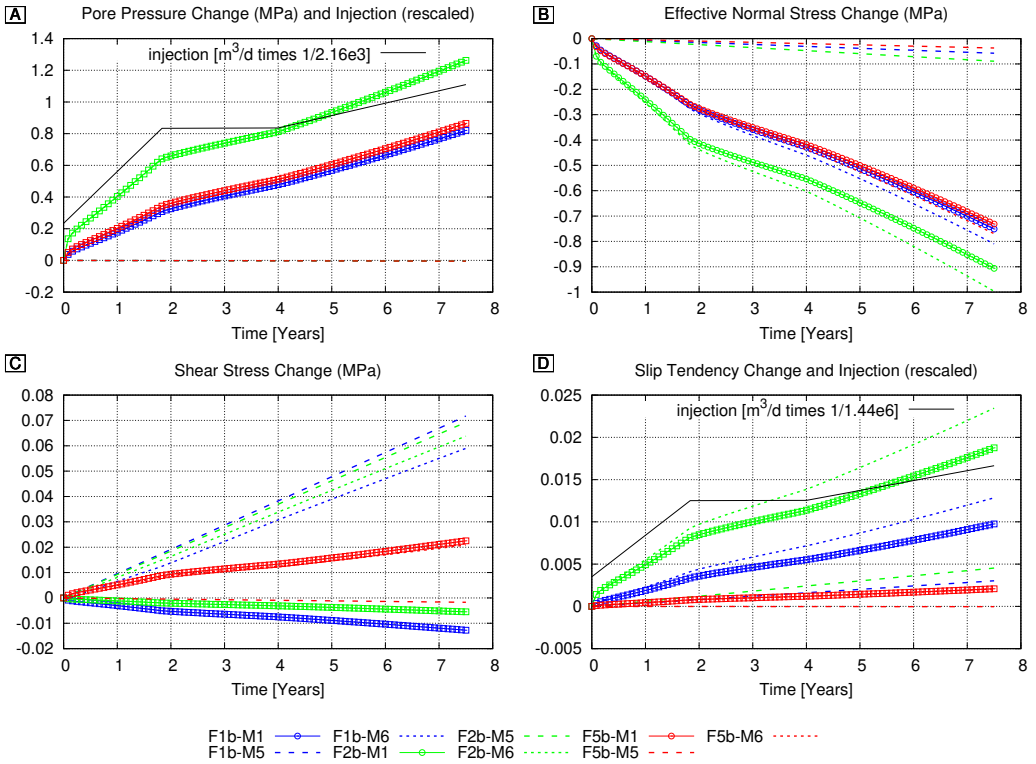

Figure 9: Comparison between the Model-1 (M1), Model-5 (M5) and Model-4 (M6) results. The time evolution of the changes in (A) pore pressure, (B) effective normal stress, (C) shear stress and (D) slip tendency is here shown only for the mid point (b) on the F1, F2 and F5 faults (see Figure 3b for The black line represents the fluid injection rates, rescaled in order to fit with the other quantities in the graph. the locations).

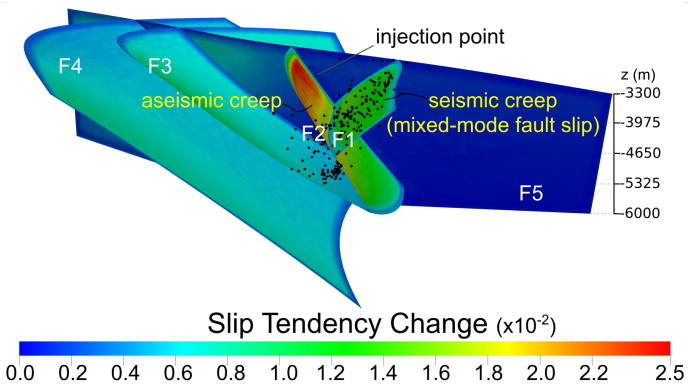

Figure 10: Mixed-mode fault slip model proposed to explain the induced seismicity in the Val d'Agri oilfield. F2 fault reactivates with an aseismic creeping deformation, while the F1 fault reactivates with a seismic creeping deformation. The plot shows the slip tendency change computed at the end of the simulation of the Model-6, where both the tectonic loading and fluid injection is simulated. Black dots indicate seismic events from June 2006 to December 2013, taken from the work of Improta et al. (2017).

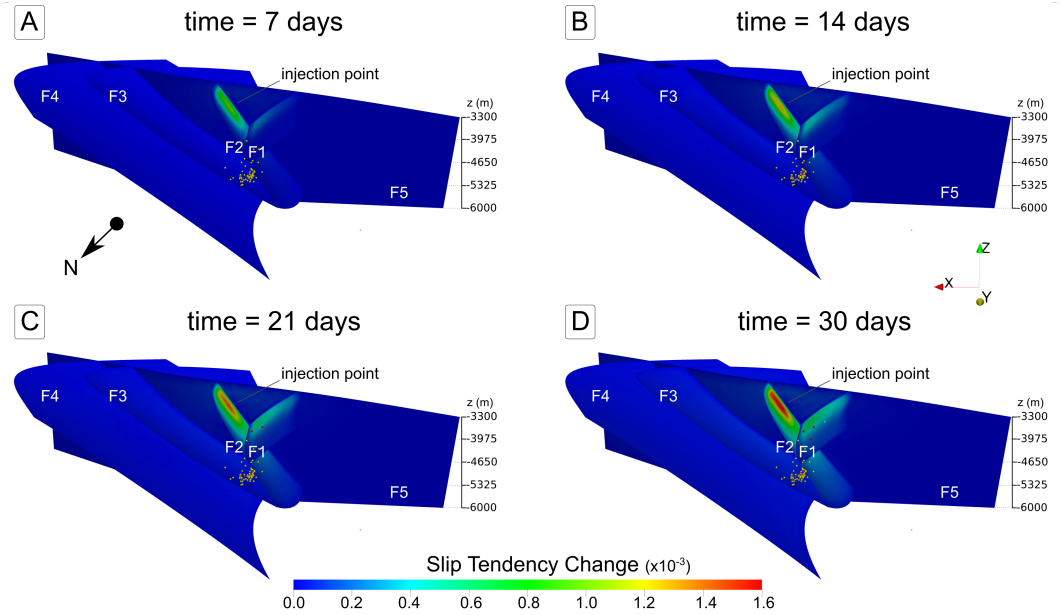

Figure 11: Time evolution of the microseismicity and slip tendency change computed in the first 30 days of the simulation. Yellow, pink, red and white dots indicate seismic events after 7, 14, 21 and 30 days respectively from the beginning of the fluid-injection in the CM2 well (Improta et al., 2017).

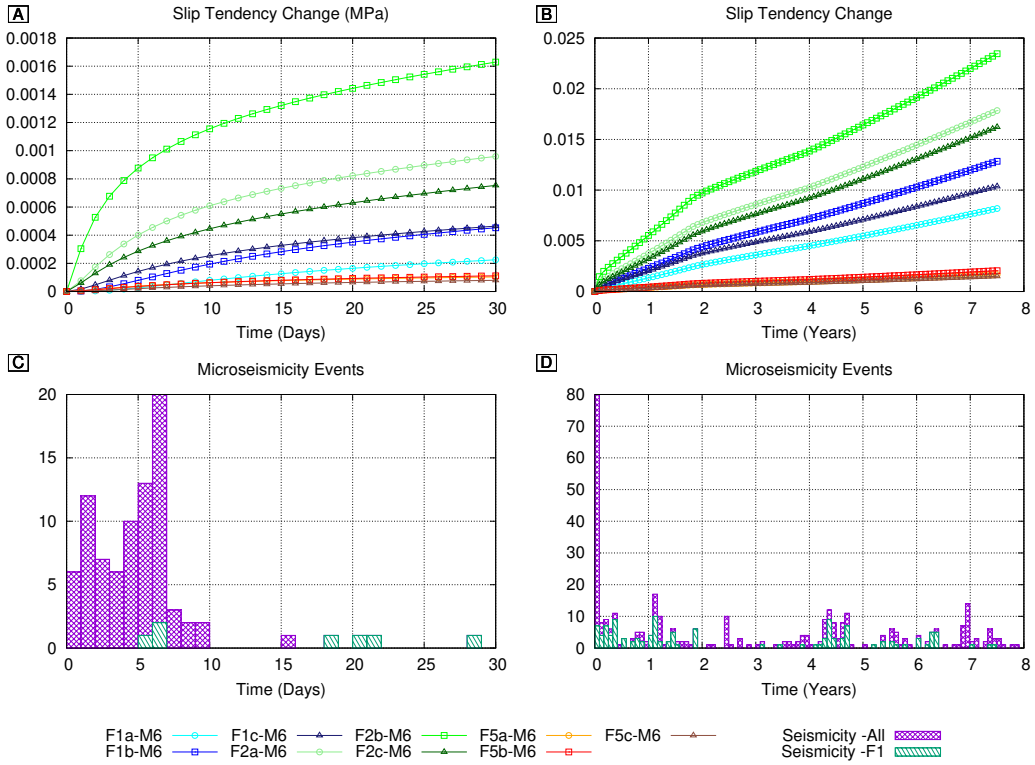

Figure 12: Comparison between the slip tendency change computed in the Model-6 (A) and the microseismicity (C) in the first 30 days. The same comparison is shown in figures (B) and (D) but for the entire duration of the simulation (7.6 years). here, the values of slip tendency change are shown for different points located on the F1, F2 and F3 faults (see location in Figure 3b). The purple and green histograms show all the seismic events and only those located on the F1 fault respectively, that occurred from 2 June 2006 (beginning of the fluid injection) to 30 December 2013 (seismic data from Improta et al., 2017)